Illusion electromagnetics for free-standing objects using passive lossless metasurfaces

Do-Hoon Kwon *

Department of Electrical and Computer Engineering, University of Massachusetts Amherst, Amherst, Massachusetts 01003, USA

(Received 20 April 2020; revised manuscript received 25 May 2020; accepted 28 May 2020; published 12 June 2020)

An electromagnetic illusion technique for free-standing objects for far-field observation using passive lossless metasurfaces is presented. Over a closed surface, the electric and magnetic surface currents needed for generating the scattered fields associated with a given physical scatterer are obtained using the surface equivalence principle. The closed surface defines an impenetrable metasurface characterized by surface impedance. A set of auxiliary evanescent surface waves are introduced and optimized over the entire surface to make the metasurface pointwise passive and lossless. Example 2D designs in TE polarization show that desired scattered fields are established immediately away from the illusion device surface. The illusion metasurfaces may be realized as tensor gradient metasurfaces.

DOI: 10.1103/PhysRevB.101.235135

I. INTRODUCTION

Electromagnetic illusion or camouflaging refers to deliberately changing the native scattering response of an object to that of a different object for a given excitation. A sensor that is close to or far from the camouflaged object would be deceived into misidentifying the object under electromagnetic probing. The most prominent example of illusion is invisibility cloaking [1–17], where the target electromagnetic scattering response is that of an empty ambient space. Transformation optics (TO)-based cloaks utilize a spatial mapping between physical and virtual spaces to find the cloak medium parameters [1–3], which are anisotropic and inhomogeneous as well as being both electric and magnetic. While effective for arbitrary illumination, TO-based cloaks exhibit extreme medium parameter values and their sizes tend to be substantial compared with the cloaked volume. Ground-plane, or carpet, cloaks based on quasiconformal TO lead to all-dielectric designs for objects placed on a ground plane [4]. Still, the cloak dimensions are often much larger than the concealed bump on the ground [5–8]. Skin or mantle cloaks are based on a scattering cancellation principle, where the induced polarization of the skin is designed to cancel the dominant scattering term of the object [9,10]. While a thin surface can achieve cloaking and a conformal profile is feasible, the effectiveness is limited to small scatterers in the quasistatic regime [11,12]. Metasurface carpet cloaks reconstruct the scattered wave using a conformal reflecting surface with a custom position-dependent reflection phase distribution [13–16]. Thin conformal surfaces for large bumps on a ground plane can be realized, but such metasurface cloaks can be designed for a specific given illumination. Furthermore, they are not effective for ground bumps under a grazing illumination or for free-standing objects, which cast a shadow. In Ref. [17], a tensor metasurface cloak design was introduced for large free-standing objects utilizing auxiliary surface waves (SWs), which carry power from the lit side to the shadow side before reconstructing the incident wave behind the scatterer.

Synthesizing nonzero scattering of a target configuration leads to illusion. Coordinate transformation was applied to find an illusion medium to convert the scattering of a conductor cylinder to that of a dielectric cylinder in Ref. [18]. The full-parameter cloak in Ref. [3] can be considered a TO-based illusion device that reduces a 2D area to a 1D line, which does not scatter an edge-on illumination in the appropriate polarization. As an extension of the scattering cancellation approach to illusion, scattering manipulation of a cylindrical object to another of different dimensions and materials has been shown in 2D [19,20] and quasi-3D scenarios [21] in the quasistatic regime. For bumps in a ground plane, conformal metasurfaces with gradient reflection phases have been reported to synthesize reflection from those of different shapes [22,23]. Illusion devices in each category based on TO, scattering-cancellation, and metasurface ground-plane cloak approaches inherit the challenges and limitations associated with their cloak counterparts with respect to device dimensions, object dimensions, and the applicability to free-standing objects. Recently, illusion mechanisms for penetrable cylindrical metasurfaces have been presented in terms of effective polarizability tensors [24].

In this paper, a design technique for illusion devices applicable to large free-standing objects is presented as electromagnetically impenetrable surfaces characterized by the passive lossless surface reactance tensor. A position-dependent reactance surface is designed such that the scattered fields match those generated by a target object. Specifically, 2D cylindrical illusion device designs are presented to synthesize scattering by objects of different shapes or materials subject to a plane- or cylindrical-wave illumination. Over the cylindrical illusion device surface, the surface impedance is determined such that the induced electric and magnetic surface currents generate the scattered fields associated with the target object. As such a surface is not guaranteed to be pointwise passive, evanescent SWs bound to the illusion device surface are

*dhkwon@umass.edu

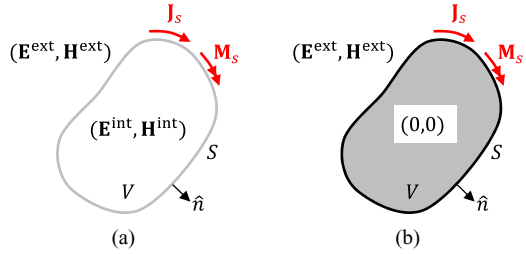

FIG. 1. Surface equivalence principle. (a) Field pairs $(\mathbf{E}^{\text{ext}}, \mathbf{H}^{\text{ext}})$ and $(\mathbf{E}^{\text{int}}, \mathbf{H}^{\text{int}})$ in the regions external and internal to a closed surface S. The discontinuities in E and H fields across S result in electric and magnetic surface currents, $\mathbf{J}_s$ and $\mathbf{M}_s$. (b) An equivalent configuration for the external region when null fields are chosen for the internal region.

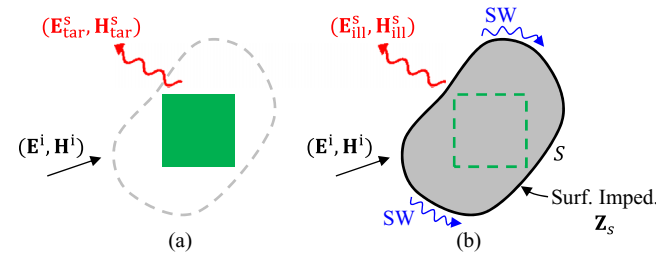

FIG. 2. Design of an illusion device. (a) A target configuration with scattered fields $(\mathbf{E}^{\text{s}}_{\text{tar}}, \mathbf{H}^{\text{s}}_{\text{tar}})$. (b) An illusion device having an impenetrable bounding surface S with scattered fields $(\mathbf{E}^{\text{s}}_{\text{ill}}, \mathbf{H}^{\text{s}}_{\text{ill}})$ on and outside S.

introduced and optimized such that the entire illusion surface becomes passive everywhere. This purposeful introduction of SWs was proposed for penetrable Ω-bianisotropic metasurfaces in realizing perfect reflectors and refractors [25,26]. The approach was extended to impenetrable surfaces for applications to anomalous reflection [27,28], cloaking [17], and leaky-wave radiation [29]. In this work, cylindrical illusion devices and orthogonally polarized SWs are treated to demonstrate the design technique. The resulting designs characterized in terms of the tensor surface reactance are validated using full-wave simulations.

II. ILLUSION VIA SURFACE EQUIVALENCE USING PASSIVE SURFACES

Given a closed surface S bounding a volume V that separates space into the external and internal regions, the surface equivalence principle [30] allows manipulating the source and material configurations of one region without affecting the fields in the other region. Figure 1(a) illustrates electric and magnetic field pairs, $(\mathbf{E}^{\text{ext}}, \mathbf{H}^{\text{ext}})$ and $(\mathbf{E}^{\text{int}}, \mathbf{H}^{\text{int}})$, external and internal to S, respectively. Each is a fully Maxwellian field pair in its region. The boundary conditions on S demands the presence of an electric surface current $\mathbf{J}_s$ and a magnetic surface current $\mathbf{M}_s$ given by

$$\mathbf{J}_s = \hat{n} \times (\mathbf{H}^{\text{ext}} - \mathbf{H}^{\text{int}}), \quad \mathbf{M}_s = (\mathbf{E}^{\text{ext}} - \mathbf{E}^{\text{int}}) \times \hat{n}, \tag{1}$$

where $\hat{n}$ is the outward unit normal. The surface S can be of either physical (e.g., an interface between two different media) or imaginary (e.g., an imaginary surface in an ambient medium) nature. For the external region, making S an impenetrable surface renders $(\mathbf{E}^{\text{int}}, \mathbf{H}^{\text{int}}) = (0, 0)$, modifying $\mathbf{J}_s$ and $\mathbf{M}_s$ accordingly via (1). Shown in Fig. 1(b), this is known as Love's equivalence.

In recent years, the surface equivalence principle has been used to design functional electromagnetic surfaces, or metasurfaces, for a variety of waveform control applications. They include Huygens' metasurfaces for reflectionless beam refraction [31,32] and directive beam forming [33], metasurface carpet cloaks [13], and optical metasurfaces for lensing and cloaking [34]. They synthesize physical meta-atoms to induce a desired set of polarization currents upon illumination by external sources. In contrast, active metasurface cloaking [35] and Huygens' box [36] have been reported based on direct synthesis of surface currents using active sources.

In this work, the surface equivalence principle is applied to achieve an illusion effect. The target configuration that is desired to be reproduced using an illusion device is illustrated in Fig. 2(a), which creates a scattered field pair $(\mathbf{E}^{\text{s}}_{\text{tar}}, \mathbf{H}^{\text{s}}_{\text{tar}})$ upon excitation by an incident field pair $(\mathbf{E}^{\text{i}}, \mathbf{H}^{\text{i}})$. A physical illusion device configuration is shown in Fig. 2(b). The illusion device is a volume V having an impenetrable surface S that contains the target object. The illusion device generates $(\mathbf{E}^{\text{s}}_{\text{ill}}, \mathbf{H}^{\text{s}}_{\text{ill}})$ on and outside S. The surface is characterized in general by a surface impedance tensor $\mathbf{Z}_s$. For the total fields in Fig. 2(b), $\mathbf{E} = \mathbf{E}^{\text{i}} + \mathbf{E}^{\text{s}}_{\text{ill}}$ and $\mathbf{H} = \mathbf{H}^{\text{i}} + \mathbf{H}^{\text{s}}_{\text{ill}}$, S is characterized by the impedance boundary condition

$$\mathbf{E}_t = \mathbf{Z}_s \mathbf{J}_s = \mathbf{Z}_s \hat{n} \times \mathbf{H}_t, \tag{2}$$

where $\mathbf{E}_t = \mathbf{E} - \hat{n}(\hat{n} \cdot \mathbf{E})$, $\mathbf{H}_t = \mathbf{H} - \hat{n}(\hat{n} \cdot \mathbf{H})$ are the respective fields tangential to the surface, and $\mathbf{M}_s = \mathbf{E}_t \times \hat{n}$. At a given frequency, illusion device design reduces to synthesis of the position-dependent surface impedance $\mathbf{Z}_s$ such that $(\mathbf{E}^{\text{s}}_{\text{ill}}, \mathbf{H}^{\text{s}}_{\text{ill}})$ approaches $(\mathbf{E}^{\text{s}}_{\text{tar}}, \mathbf{H}^{\text{s}}_{\text{tar}})$ outside S. If $(\mathbf{E}^{\text{s}}_{\text{ill}}, \mathbf{H}^{\text{s}}_{\text{ill}}) = (\mathbf{E}^{\text{s}}_{\text{tar}}, \mathbf{H}^{\text{s}}_{\text{tar}})$ everywhere, it is near-field, or perfect, illusion. If the equality holds far away from S, as in radar cross section (RCS) observations, it is far-field illusion.

Let us consider a lossless object for the target configuration. It may be possible to design a pointwise-lossless illusion surface S. While the overall power through S is zero, a simple enforcement of $(\mathbf{E}^{\text{s}}_{\text{ill}}, \mathbf{H}^{\text{s}}_{\text{ill}}) = (\mathbf{E}^{\text{s}}_{\text{tar}}, \mathbf{H}^{\text{s}}_{\text{tar}})$ on S typically leads to a surface made up of locally active or lossy parts [24,37]. As device realization incorporating active constituents is challenging, designs that allow realization using passive materials are preferable. For overall power-preserved wave transformations, a pointwise lossless surface can be obtained by introducing an optimal set of SWs that carry and distribute power over S, as illustrated in Fig. 2(b). For transmissive surfaces, zero loss at a surface point is characterized by the local power conservation [25]. For impenetrable surfaces, a lossless surface point is associated with a vanishing Poynting vector component in the surface normal direction [17], i.e.,

$$S_n(\mathbf{r}) = \hat{n} \cdot \mathbf{S}(\mathbf{r}) = 0, \ \mathbf{r} \in S, \tag{3}$$

where $\mathbf{S} = \text{Re}\{\mathbf{E} \times \mathbf{H}^*\}/2$ is the time-average Poynting vector. Hence, we aim to design passive illusion devices for lossless target configurations by synthesizing a surface impedance $\mathbf{Z}_s$ that induces a desired set of surface currents $\mathbf{J}_s$ and $\mathbf{M}_s$,

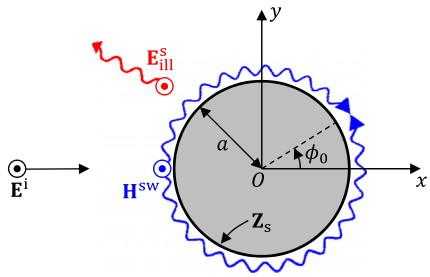

FIG. 3. A circular cylindrical illusion device in the TE polarization. An impenetrable cylindrical bounding surface of radius a scatters an incident wave and creates a desired illusion wave. TM-polarized SWs are induced on the surface. The configuration is uniform and invariant in z.

or equivalently $\mathbf{E}_t$ and $\mathbf{H}_t$, on S under a known illumination. Pointwise passivity is achieved by introducing and optimizing SWs on S, propagating along the surface, for satisfying (3) everywhere.

Illusion for external regions realized using an impenetrable surface S is treated in this work for allowing a possibility to hide an object inside S. Null fields inside S allow the surface to be characterized by a surface impedance tensor. Illusion for internal regions is obtained using the surface equivalence principle, where a target field pair is to be synthesized inside S. With the primary sources being located outside the surface, an internal illusion device becomes a penetrable, or transmissive, surface S. It is characterized by the electric admittance, magnetic impedance, magnetoelectric coupling, and electromagnetic coupling tensors, all of which are 2×2 tensors in general. In fact, many planar transmissive metasurfaces for wave transformation applications may be considered internal illusion devices, where S is an infinite planar surface that closes at infinity.

III. PASSIVE CYLINDRICAL SURFACE SYNTHESIS FOR FAR-FIELD ILLUSION

For quantitative illusion device designs in terms of the surface impedance of the bounding surfaces, let us consider 2D scattering in TE polarization (the E field along the axis of uniformity). Figure 3 shows a cylindrical illusion device of radius a subject to a TE-polarized illumination from the $-x$-axis direction. In standard (ρ, ϕ, z) cylindrical coordinates, we choose a cylindrical device in this work because fields in $\rho \geqslant a$ can be efficiently determined from the tangential fields at $\rho = a$ in terms of cylindrical harmonics. For a closed surface of arbitrary cross section, knowledge of the tangential E or H field on S uniquely determines all fields on and outside S using electromagnetic Green's functions. However, field evaluations are more involved in comparison. For the purpose of finding passive designs, TM-polarized SWs are introduced and optimized. While they lead to tensor surface impedances, cross-polarized SWs permit straightforward analytical designs [27] or numerical optimizations [17] in enforcing the design principle given by (3). It should be possible to introduce co-polarized SWs in achieving (3) as was done for planar surfaces [28,29], but SW optimizations are expected to be complex, involving multiple spatial harmonics.

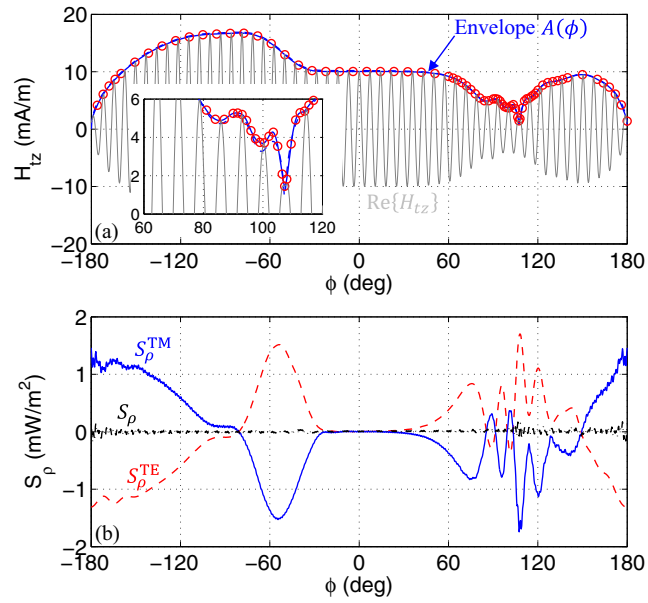

FIG. 4. Introduction and optimization of the TM-polarized SW. (a) The optimized envelope $A(\phi)$ and the resulting $H_{tz}(\phi)$. (b) The Poynting vector components in the surface normal direction for the TE, TM, and total fields.

Consider time-harmonic scattering with an $e^{j\omega t}$ time convention. For a desired target configuration in TE polarization, the scattered fields are known from either analytical solutions or numerical simulations over the illusion surface S, i.e., at $\rho = a$ in $\phi \in [-\pi, \pi]$. Let the tangential components of the total TE fields be denoted by $E_{tz}(\phi) = E_z(\rho = a, \phi)$ and $H_{t\phi}(\phi) = H_\phi(\rho = a, \phi)$. The time-average Poynting vector component in the surface normal direction is $S_\rho^{\mathrm{TE}} = -\mathrm{Re}\{E_{tz}H_{t\phi}^*\}/2$. Let us use an example design for a target of a perfect electric conductor (PEC) cylinder with an equilateral triangular cross section presented in Sec. IV A to detail the design technique. For a triangular cylinder of a side of $3\sqrt{3}\lambda$ (λ = free-space wavelength) subject to a unit plane-wave propagating in the $+x$ direction given by $\mathbf{E}^{\mathrm{i}} = \hat{z}e^{-jkx}$ V/m (k = free-space wave number), full-wave simulation [Fig. 6(a)] finds E_{tz} and $H_{t\phi}$ on a cylindrical surface of $a = 4\lambda$. Its associated radial power density, S_ρ^{TE}, is shown in Fig. 4(b).

As the surface characterized solely by the TE-mode fields is either active ($S_\rho^{\mathrm{TE}} > 0$) or lossy ($S_\rho^{\mathrm{TE}} < 0$) depending on location, we introduce TM-polarized SWs. The TM-mode fields are completely characterized in terms of the tangential z-component of its magnetic field, $H_{tz}(\phi) = H_z(\rho = a, \phi)$. Using an envelope function $A(\phi)$ to be determined, we define $H_{tz}(\phi)$ as

$$H_{tz}(\phi) = \begin{cases} A(\phi)e^{-jk_c a\phi}, & -\pi \leqslant \phi < \phi_0 \\ A(\phi)e^{jk_c a\phi}, & \phi_0 \leqslant \phi < \pi \end{cases}, \tag{4}$$

where k_c chosen in the evanescent range ($k_c > k$) is the "carrier" propagation constant that binds the TM fields to the cylinder surface. Remember that the SWs are introduced to distribute power over S to make the surface lossless everywhere. The angle ϕ_0 is determined such that the two ranges $\phi \in [-\pi, \phi_0]$ and $\phi \in [\phi_0, \pi]$ are individually power-neutral,

i.e., the net power penetrating S in each range is zero. Two oppositely propagating SWs that initiate at $\phi = \pi$ meet each other and vanish at $\phi = \phi_0$, as described in Fig. 3. This angle can be found by solving

$$I(\phi) = \int_{-\pi}^{\phi} S_\rho^{\mathrm{TE}}(\phi') a d\phi' = 0. \tag{5}$$

For the example design, it is found that $\phi_0 = 107.3^\circ$.

The tangential E field associated with $H_{tz}(\phi)$ can be found using field expansions in cylindrical harmonics. It can be shown that the ϕ component of the E field on the surface, $E_{t\phi}(\phi) = E_\phi(\rho = a, \phi)$, is expressed as

$$E_{t\phi}(\phi) = j\eta \sum_{n=-\infty}^{\infty} a_n \frac{H_n^{(2)\prime}(ka)}{H_n^{(2)}(ka)} e^{jn\phi}, \tag{6}$$

where $\eta \approx 377\,\Omega$ is the free-space intrinsic impedance and $H_n^{(2)}(\cdot)$ is the Hankel function of order n of the second kind. The expansion coefficient a_n is given by

$$a_n = \frac{1}{2\pi} \int_{-\pi}^{\pi} H_{tz}(\phi) e^{-jn\phi} d\phi. \tag{7}$$

The power density for the TM-mode fields is $S_\rho^{\mathrm{TM}} = \mathrm{Re}\{E_{t\phi} H_{tz}^*\}/2$ and it is completely specified by $A(\phi)$.

Owing to the orthogonality between TE and TM modes, the local condition (3) for zero loss becomes

$$S_\rho(\phi) = S_\rho^{\mathrm{TE}}(\phi) + S_\rho^{\mathrm{TM}}(\phi) = 0. \tag{8}$$

Now, designing a lossless impedance surface becomes determining the envelope $A(\phi)$ in (4) such that (8) is satisfied everywhere. Using a total of N_c control point angles ϕ_i, the sampled values $A(\phi_i)$ $(i = 1, \ldots, N_c)$ define the envelope via interpolation. For the example design, Fig. 4(a) shows ϕ_i and $A(\phi_i)$ (red circles) for $N_c = 74$ control points. A finer control point density is used over $\phi \in [90^\circ, 120^\circ]$, where the envelope changes rapidly as detailed in the inset. In optimizing $A(\phi)$ via numerical optimization, an approximate envelope profile can serve as a good initial guess. Based on power balance between the attenuated TM-polarized SW and the TE-polarized space wave leaving the surface over a differential arc length $d\ell' = a d\phi'$, an approximate envelope can be found as

$$A_{\mathrm{approx}}(\phi) = \left| -\frac{4k\alpha_c}{k_c \eta} \int_{-\pi}^{\phi} S_\rho^{\mathrm{TE}}(\phi') a d\phi' \right|^{1/2}, \tag{9}$$

where $\alpha_c = \sqrt{k_c^2 - k^2}$ is the attenuation constant of the SW in the radial direction. Its accuracy improves for a slowly-varying envelope and a large radius a.

As (8) cannot be satisfied exactly everywhere on S for a typical design, an error metric can be defined and minimized for its approximate satisfaction in an average sense. In this work, a relative square error is defined as

$$e_{\mathrm{sq}} = \frac{1}{e_0} \int_{-\pi}^{\pi} |S_\rho(\phi)|^2 d\phi, \; e_0 = \int_{-\pi}^{\pi} \left| S_\rho^{\mathrm{TE}}(\phi) \right|^2 d\phi. \tag{10}$$

Using the *fminsearch* function in MATLAB, the envelope profile is optimized for minimizing e_{sq}, starting from (9). Using a choice of $k_c = 2k$, a minimized error value of $e_{\mathrm{sq}} = 1.77 \times 10^{-3}$ is reached for the example design. The optimized envelop is plotted in Fig. 4(a). Also shown as a blue dashed curve is the initial guess (9), which is observed to be very close to the optimized profile. The optimized TM-mode power profile, S_ρ^{TM}, is shown in Fig. 4(b). It successfully cancels S_ρ^{TE}, bringing the total power density close to zero everywhere.

The impedance boundary condition (2) is used to find the surface impedance $\mathbf{Z}_s$ of the illusion device surface S. Toward obtaining a lossless surface, a tensor surface impedance of the form

$$\mathbf{Z}_s = j\mathbf{X}_s = j \begin{bmatrix} X_{\phi\phi} & X_{\phi z} \\ X_{z\phi} & X_{zz} \end{bmatrix} \tag{11}$$

can be adopted, where $\mathbf{X}_s$ is the surface reactance tensor with real-valued elements. The four reactance elements are uniquely determined in terms of the four tangential field components—E_{tz}, $E_{t\phi}$, H_{tz}, and $H_{t\phi}$ [17]. However, at positions where $S_\rho(\phi)$ is close to but not exactly equal to zero, the resulting 2×2 surface reactance does not represent lossless reciprocal points, albeit at a minor level. Since realization using reciprocal constituents is desirable in addition to being lossless, we find an approximate solution to (2) while limiting $\mathbf{X}_s$ to symmetric tensors. A symmetric reactance tensor has three independent elements and there are four real-valued linear equations. Here we adopt a least-squares solution for the reactance tensor, written as

$$\mathbf{X}_s^{\mathrm{lsq}} = \begin{bmatrix} X_{\phi\phi}^{\mathrm{lsq}} & X_{\phi z}^{\mathrm{lsq}} \\ X_{z\phi}^{\mathrm{lsq}} & X_{zz}^{\mathrm{lsq}} \end{bmatrix}, \; X_{z\phi}^{\mathrm{lsq}} = X_{\phi z}^{\mathrm{lsq}}. \tag{12}$$

The three independent elements are found by solving the normal equation derived from (2) [17].

For the example illusion synthesis for a PEC cylinder, the elements of $\mathbf{X}_s^{\mathrm{lsq}}$ are shown in Fig. 5. They represent a highly anisotropic and inhomogeneous surface. The fast reactance variation in $\ell/\lambda \in [0, 7.49]$ $(\phi \in [0, \phi_0])$ is associated with the local wave vectors for the TE-polarized space wave and the TM-polarized SW pointing in opposite directions. Nevertheless, the impedance is reactive and reciprocal, allowing physical realization using passive, reciprocal constituents.

While an ideal illusion surface accompanied by an exact satisfaction of (8) reproduces the exact target fields in the TE polarization on and outside S, presence of the TM SW fields in this work makes the illusion effect accurate at far distances. An observer that is on or in the extreme near zone of S will be able to detect field deviations from $(\mathbf{E}_{\mathrm{tar}}^{\mathrm{s}}, \mathbf{H}_{\mathrm{tar}}^{\mathrm{s}})$. However, such deviations should practically disappear away from the immediate vicinity of the illusion surface.

IV. NUMERICAL EXAMPLES

A. A PEC object under plane-wave illumination

Consider a PEC cylinder of a triangular cross section with a base parallel with the x-axis and the centroid positioned at the coordinate origin. It is subject to a plane-wave illumination given by $\mathbf{E}^{\mathrm{i}} = \hat{z} e^{-jkx}\,\mathrm{V/m}$ at frequency $f = 300\,\mathrm{MHz}$ $(\lambda = 1\,\mathrm{m})$. The side of the equilateral triangle is $3\sqrt{3}\lambda$ and the illusion device is a circular cylinder with radius $a = 4\lambda$. The illusion device design has been detailed in Sec. III. Scattering by the target is analyzed using COMSOL MULTIPHYSICS and a snapshot of $E_z(x, y)$ is plotted in Fig. 6(a). A strong specular

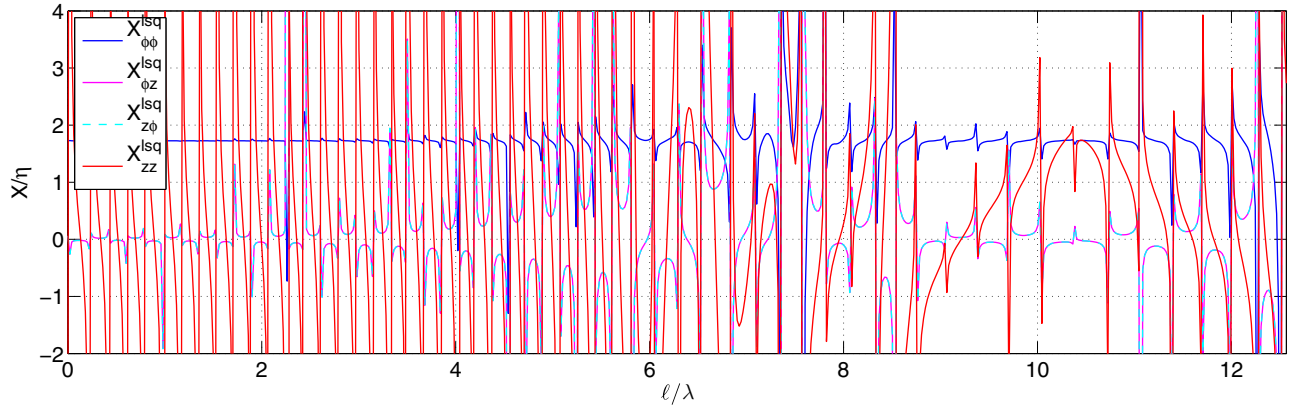

FIG. 5. The surface reactance tensor elements for the illusion device for a triangular PEC cylinder. For clarity, only the parameters for the top half of the cylindrical surface are shown for the arc length variable $\ell = a\phi$ over $0 \leqslant \phi < \pi$.

reflection toward $\phi = 120^\circ$ is observed and a deep shadow is cast in the forward direction.

The performance of the illusion device design is simulated using COMSOL by enforcing the tensor surface reactance $\mathbf{X}_s^{\text{lsq}}$ in Fig. 5 mathematically at $\rho = a$. A snapshot of the resulting E field distribution is shown in Fig. 6(b). Outside the illusion surface, a distribution that is visually identical to that in the target configuration is observed, including the strong specular reflection and the deep shadow. This confirms a successful illusion function on a qualitative level.

Figure 7(a) shows a snapshot of $H_z(x, y)$, the H field component of the TM-polarized SW introduced in the design. As intended, SWs tightly bound to the illusion surface are induced, carrying and distributing power along the surface to make it passive and lossless everywhere. The strongest $|H_{tz}|$ value around 16.9 mA/m observed near $\phi = -90^\circ$ is consistent with the designed value shown in Fig. 4(a). For quantitative comparison of the far-zone illusion performance, the 2D bistatic scattering width σ_{2D} [30] is compared in Fig. 7(b) between the target and illusion device. The illusion device reproduces the two main scattering lobes at $\phi = 0^\circ$, 120° accurately. Minor deviations appear away from these main lobes, but the overall angle dependence is accurately reproduced.

A typical metasurface realization of the synthesized surface reactance comprises an array of spatially varying subwavelength resonators. The effect of reactance discretization on illusion performance may be gauged by using a staircase-approximated reactance profile in simulation. The surface reactance over an arc length of $\Delta\ell$ can be uniformly set to the value evaluated at the half-way point along the arc. This can be achieved by defining a sampling angle ϕ_s by

$$\phi_s = \left(\left\lfloor \frac{\phi}{\Delta\phi} \right\rfloor + \frac{1}{2}\right)\Delta\phi, \quad \Delta\phi = \frac{\Delta\ell}{a} \tag{13}$$

and enforcing $\mathbf{X}_s^{\text{lsq}}(\phi_s)$ on the cylinder surface. The tensor reactance in Fig. 5 has been discretized using different discretization intervals. Scattering simulation results using a discretized reactance for four different values of $\Delta\ell$ are compared with the continuous reactance case in Fig. 8. With finer discretizations (decreasing $\Delta\ell$), the overall deviation of σ_{2D} increases from the continuous variation case. In particular,

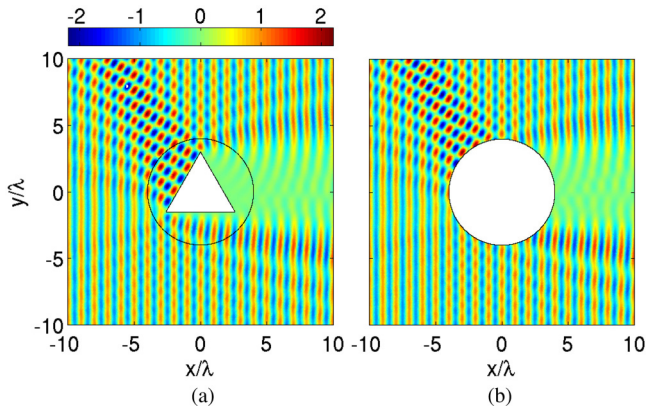

FIG. 6. Distributions of $E_z(x, y)$ in V/m for a triangular PEC cylinder and its illusion device. The target is a cylinder of an equilateral triangular cross section with a side of $3\sqrt{3}\lambda$. (a) An E-field snapshot for the target cylinder. The black circle indicates the imaginary contour of the illusion device to be designed. (b) An E-field snapshot for the cylindrical illusion device of $a = 4\lambda$.

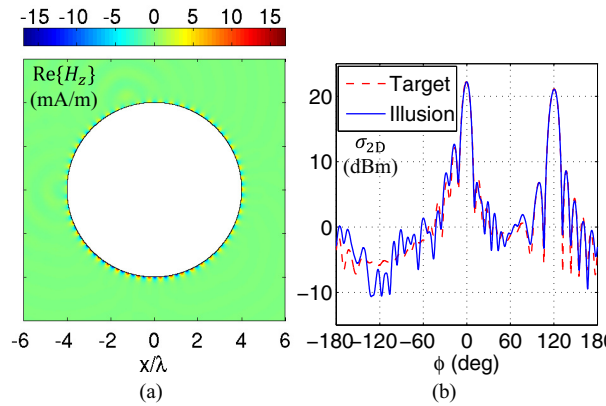

FIG. 7. Illusion characteristics for the triangular PEC cylinder. (a) A snapshot of H_z for the illusion device. (b) Comparison of σ_{2D} between the target cylinder and the illusion device.

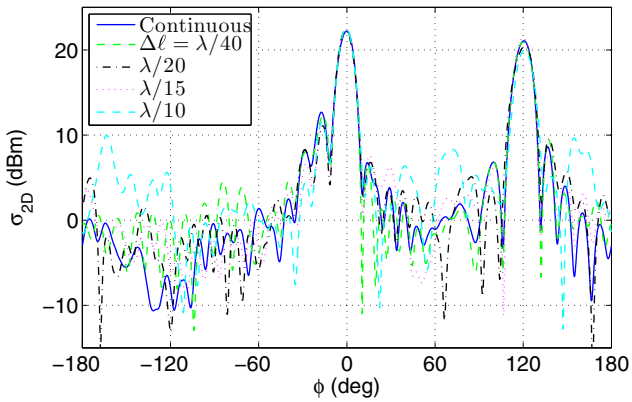

FIG. 8. Comparison of σ_{2D} for different discretization intervals of the tensor surface reactance for the cylindrical illusion device.

a coarse discretization associated with $\Delta\ell = \lambda/10$ causes a few significant minor scattering lobes to appear. However, the direction and strength of the scattering lobe at $\phi = 120^\circ$ associated with a specular reflection are correctly reproduced by all discretizations considered. This suggests that a fine discretization in metasurface realization may not be required for reproducing strong scattering lobes.

Due to the frequency dispersion of subwavelength resonators in a physical metasurface realization, successful illusion is expected to be narrowband. The exact bandwidth property depends on the geometrical and material specifics of a physical design. Nevertheless, it is instructive to analyze the illusion performance dependence on frequency assuming a nondispersive surface reactance as a best-case scenario. Noting that an illusion characteristic of interest is unique to every scattering configuration, we find that the triangular PEC cylinder provides a frequency-consistent scattering feature that can be investigated for dispersion—formation of a strong scattering lobe at $\phi = 120^\circ$. The cylindrical illusion device is analyzed for plane-wave scattering over 270–330 MHz using $\mathbf{X}_s^{\text{lsq}}$ shown in Fig. 5 as a nondispersive surface reactance. Figure 9(a) compares the scattering width around the specular reflection direction at three different frequencies. While the

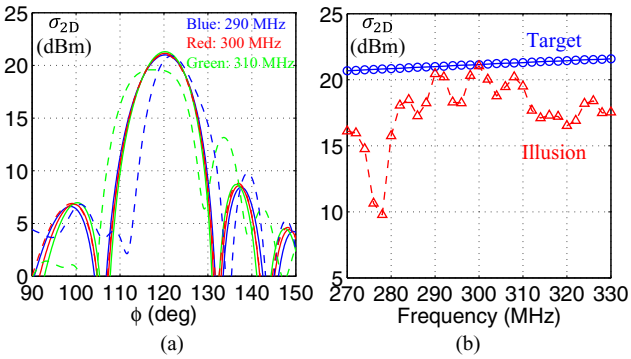

FIG. 9. Simulated dispersion characteristics of the illusion characteristics assuming ideal, frequency-independent surface reactance. (a) σ_{2D} around $\phi = 120^\circ$ at 290, 300, and 310 MHz. Solid and dashed curves represent target and illusion responses, respectively. (b) σ_{2D} at $\phi = 120^\circ$ as a function of frequency.

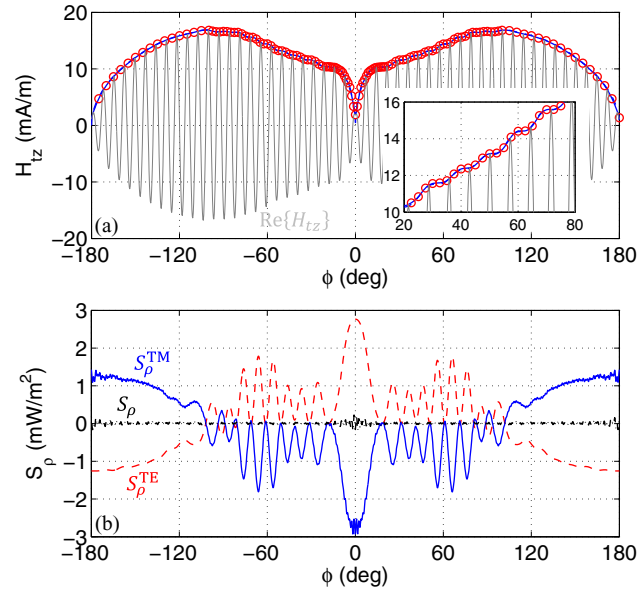

FIG. 10. Illusion surface design for a dielectric cylinder. (a) The optimized envelope $A(\phi)$ and the associated TM-polarized tangential H field component, $H_{tz}(\phi)$. (b) Radial Poynting vector components for the TE, TM, and total fields.

illusion device accurately reproduces the scattering characteristics of the target at 300 MHz, both the direction and strength of the scattering lobe slightly deviate from the target responses at 290 and 310 MHz. At $\phi = 120^\circ$, the scattering width is compared between the target and illusion device with respect to frequency in Fig. 9(b). For the target, the scattering lobe slowly strengthens with frequency as the electrical width of the flat reflecting face increases. In comparison, σ_{2D} of the illusion device oscillates and weakens away from the design frequency. Using a 3-dB criterion for scattering width reduction, the bandwidth of the illusion device for specular reflection reproduction is approximately 24 MHz, or 8%.

B. A dielectric object under plane-wave illumination

As an illusion synthesis for a penetrable body, a target of a dielectric cylinder of a square cross section subject to plane-wave illumination is considered. At $f = 300$ MHz, the side of the square cross section is $3\sqrt{2}\lambda$ and a unit plane wave illuminates along a diagonal, as shown in Fig. 11(a). The relative permittivity of the simple dielectric cylinder is $\epsilon_r = 2$. The coordinate system is set up such that the incident plane wave propagates in the $+x$-axis direction. The illusion device is a cylindrical impedance surface of a radius $a = 4\lambda$.

From scattering simulation of the target [Fig. 11(a)], the TE-polarized power density to be canceled using TM-polarized SWs is determined, as shown in Fig. 10(b) (red dash). Symmetry in the geometry and illumination gives $\phi_0 = 0$, which is also confirmed from (5) numerically. Using $k_c = 2k$, the TM-polarized H field envelope $A(\phi)$ is optimized using $N_c = 129$ control points. The resulting converged error is $e_{\text{sq}} = 1.16 \times 10^{-3}$. The optimized $H_{tz}(\phi)$ is shown in Fig. 10(a) together with the ϕ-positions and

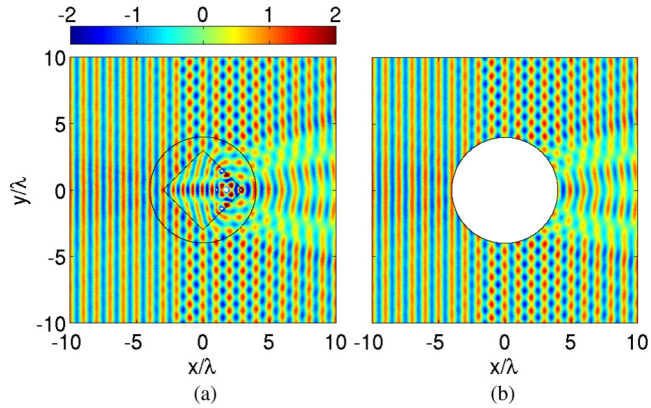

FIG. 11. Simulation results for the $E_z(x, y)$ distribution in V/m for a dielectric cylinder and its illusion device. The target is a dielectric cylinder of relative permittivity $\epsilon_r = 2$ with a square cross section of a 6λ diagonal. A unit-amplitude plane wave propagating in the $+x$-axis direction illuminates the cylinder. (a) A snapshot of $E_z(x, y)$ for the target cylinder. (b) A snapshot of $E_z(x, y)$ for the cylindrical illusion device of $a = 4\lambda$.

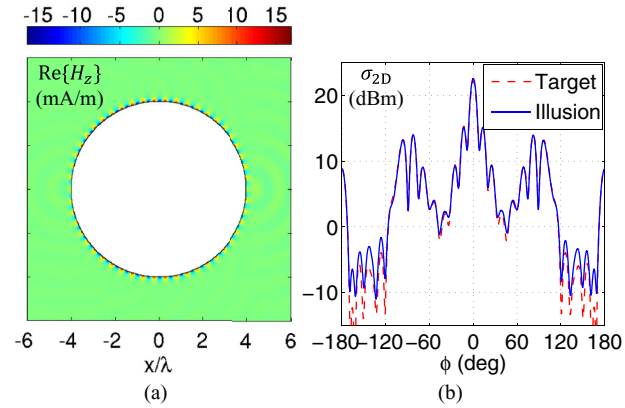

FIG. 12. Illusion characteristics for the square dielectric cylinder. (a) A snapshot of H_z for the illusion device. (b) Comparison of σ_{2D} for the target cylinder and illusion device.

values of the envelope samples. Fine small-scale variations of S_ρ^{TE} in $|\phi| \in [20°, 100°]$ necessitate a small sampling interval of 0.175λ along the arc. The inset shows the fine amplitude variation captured by the high sampling density. Fine sampling is also needed to bring S_ρ close to zero near $\phi = 0$, where the envelope changes precipitously. The optimized envelope is close to the initial guess (blue dash-dot) given by (9) assuming a slowly-varying envelope. Overall, Fig. 10(b) shows that the no-loss condition (8) is approximately satisfied over the entire surface.

The tensor surface reactance that describes a pointwise lossless and reciprocal surface is obtained using the procedure described in Sec. III (not shown). The spatially varying surface reactance is mathematically enforced on the cylinder surface to test the illusion characteristics. For the target dielectric cylinder, a snapshot of $E_z(x, y)$ is plotted in Fig. 11(a). Unlike with the PEC cylinder in Sec. IV A, the shadow in the forward direction is partially filled due to the penetrable nature of the target. The E_z field distribution for the cylindrical illusion device is shown in Fig. 11(b). A visually identical distribution associated with the target configuration is produced, including the field penetrating the target in the forward direction.

A snapshot of the $H_z(x, y)$ distribution is plotted in Fig. 12(a). Two equally strong SWs are induced on the top and bottom halves of the cylindrical surface, as anticipated from the symmetry. The angular envelop profile of the induced H field is consistent with the design in Fig. 10(a). For quantitative comparison of the far field scattering characteristics, the 2D scattering width is compared between the target and illusion configurations in Fig. 12(b). An excellent agreement is observed, with minor differences showing at low RCS levels.

C. A PEC object under cylindrical-wave illumination

The illusion synthesis technique is not limited to plane-wave illuminations. In order to demonstrate the effectiveness of the method for incidence by other than plane waves, we consider a conducting cylinder illuminated by a cylindrical wave. Consider a PEC cylinder with a five-pointed star cross section near an electric line current [Fig. 14(a)]. At $f =$ 300 MHz, a $+\hat{z}$-directed line source carrying 1 A of current is located at $(x_s, y_s) = (-7\lambda, 0)$. The star-shaped cross section has its centroid located at O and is circumscribed by a circle of radius 3λ.

Along a circle of radius $a = 4\lambda$, the fields of the target configuration gives a power density S_ρ^{TE} shown in Fig. 13(b) (red dash). For this configuration, it is found that $\phi_0 = -106.6°$ from (5). Using $k_c = 2k$, the envelope $A(\phi)$ for the TM-polarized SW is optimized to satisfy (8) using $N_c = 92$ control points. The optimized envelope together with the control points are shown in Fig. 13(a). A fine sampling interval of 0.175λ is used in $\phi \in [-180°, -90°]$ and $[70°, 130°]$, where detailed amplitude control for S_ρ^{TM} is needed for canceling the

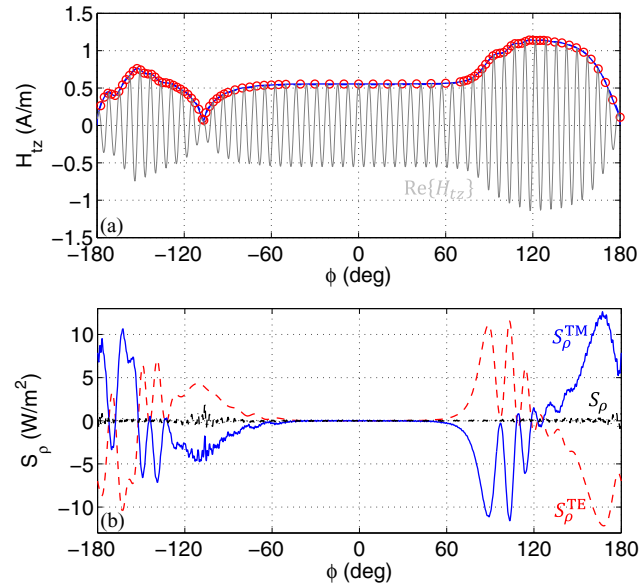

FIG. 13. Illusion surface design for line-source illumination. (a) The optimized envelope $A(\phi)$ and the resulting $H_{tz}(\phi)$. (b) Radial Poynting vector components for the TE, TM, and total fields.

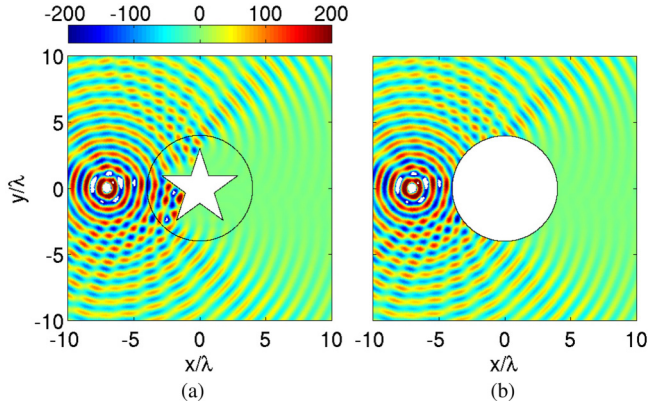

FIG. 14. Distribution of $E_z(x, y)$ in V/m for an illusion device subject to a line-source excitation. An electric line current of 1 A/m flows in the $+\hat{z}$ direction at $(x_s, y_s) = (-7\lambda, 0)$. The target is a five-pointed star-shaped PEC cylinder that is contained in a 3λ-radius circle. (a) A snapshot for the target PEC cylinder. (b) A snapshot for the cylindrical illusion device of $a = 4\lambda$. The color plots are clipped at $|E_z| = 200\,\mathrm{V/m}$.

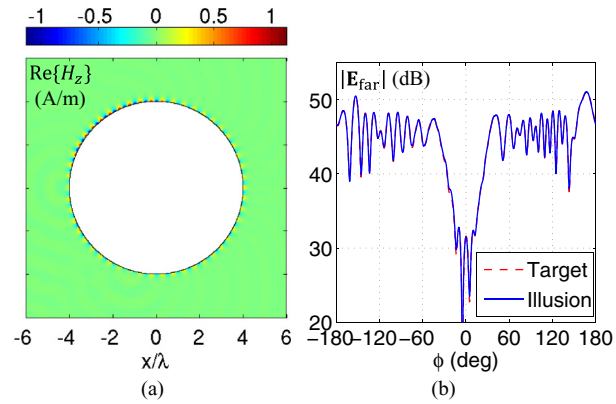

FIG. 15. Illusion characteristics for the PEC cylinder excited by a line current. (a) A snapshot of H_z for the illusion device. (b) Comparison of the far-zone E-field magnitude for the target cylinder and the illusion device with respect to the observation angle ϕ.

rapid variations in S_ρ^{TE}. A minimized error of $e_{\mathrm{sq}} = 2.08 \times 10^{-3}$ is reached.

With the optimized $A(\phi)$, the associated surface reactance tensor $\mathbf{X}_s^{\mathrm{lsq}}$ is found using the least-squares approximation (not shown). Full-wave simulation is performed using COMSOL by mathematically specifying the position-dependent surface reactance tensor at $\rho = a$. The total E-field component, $E_z(x, y)$, is plotted in Fig. 14(b) for the illusion device subject to the line-source excitation. A visually identical field distribution is obtained, including a shadow over a wide angular range around $\phi = 0$.

A snapshot of H_z is plotted in Fig. 15(a). An H field distribution shown in Fig. 13(a) is correctly induced, with strongest magnitudes observed in $\phi \in [90^\circ, 160^\circ]$. Far-zone scattering characteristics between the target and illusion device are compared in Fig. 15(b). Since RCS is defined for plane-wave illumination, a 2D scattering width is not relevant for this configuration. In 2D, a far-zone vector phasor, $\mathbf{E}_{\mathrm{far}}(\phi)$, can be defined to express the far-zone E-field distribution as

$$\mathbf{E}(\rho, \phi) = \mathbf{E}_{\mathrm{far}}(\phi)\frac{e^{-jk\rho}}{\sqrt{\rho}}. \tag{14}$$

The magnitude of $\mathbf{E}_{\mathrm{far}}$ is compared in Fig. 15(b) in log scale, where the reference value for $|\mathbf{E}_{\mathrm{far}}|$ is $1\,\mathrm{V}/\sqrt{\mathrm{m}}$ (volt per square root of meter). An excellent agreement is observed between scattering by the target and illusion device. A deep null around $\phi = 0$ and rapid angular variations in $\phi \in [60^\circ, 150^\circ]$ are accurately reproduced by the illusion device.

V. CONCLUSION

An electromagnetic illusion or camouflaging device design technique has been presented based on the surface equivalence principle. For a target scattering configuration, an illusion surface that encloses the target can be designed as an electromagnetically impenetrable surface, on which the fields from the target configuration are induced. In addition, SWs are introduced and optimized over the entire illusion surface to make the surface lossless and reciprocal everywhere. Illusion devices for 2D TE-polarized scattering scenarios have been designed in terms of the tensor surface reactance and their illusion performances have been validated using full-wave simulations. The proposed illusion surface synthesis technique promises thin realizations as opposed to TO-based illusion techniques and enables illusion for electrically large, free-standing objects.

The biggest challenge in achieving the proposed illusion is accurate realization of the inhomogeneous, anisotropic surface reactance as thin impenetrable physical structures. In the microwave regime, arrays of printed subwavelength resonators on a grounded dielectric substrate [38–40] are prime candidates. While the bandwidth property of the proposed illusion devices depends on physical realizations, the resonant nature of subwavelength inclusions in typical metasurface realizations tends to limit the effective bandwidth. However, the illusion bandwidth of individual designs should be tested against that of the target configuration.

ACKNOWLEDGMENT

This work was supported by the US Army Research Office under Grant No. W911NF-19-2-0244.

[1] J. B. Pendry, D. Schurig, and D. R. Smith, Controlling electromagnetic fields, Science **312**, 1780 (2006).

[2] D. Schurig, J. J. Mock, B. J. Justice, S. A. Cummer, J. B. Pendry, A. F. Starr, and D. R. Smith, Metamaterial electromagnetic cloak at microwave frequencies, Science **314**, 977 (2006).

[3] N. Landy and D. R. Smith, A full-parameter unidirectional metamaterial cloak for microwaves, Nat. Mater. **12**, 25 (2013).

[4] J. Li and J. B. Pendry, Hiding under the Carpet: A New Strategy for Cloaking, Phys. Rev. Lett. **101**, 203901 (2008).

[5] R. Liu, C. Ji, J. J. Mock, J. Y. Chin, T. J. Cui, and D. R. Smith, Broadband ground-plane cloak, Science **323**, 366 (2009).

[6] J. Valentine, J. Li, T. Zentgraf, G. Bartal, and X. Zhang, An optical cloak made of dielectrics, Nat. Mater. **8**, 568 (2009).

[7] H. F. Ma and T. J. Cui, Three-dimensional broadband ground-plane cloak made of metamaterials, Nat. Commun. **1**, 21 (2010).

[8] T. Ergin, N. Stenger, P. Brenner, J. B. Pendry, and M. Wegener, Three-dimensional invisibility cloak at optical wavelengths, Science **328**, 337 (2010).

[9] A. Alù and N. Engheta, Achieving transparency with plasmonic and metamaterial coatings, Phys. Rev. E **72**, 016623 (2005).

[10] A. Alù, Mantle cloak: Invisibility induced by a surface, Phys. Rev. B **80**, 245115 (2009).

[11] D. Rainwater, A. Kerkhoff, K. Merlin, J. C. Soric, G. Moreno, and A. Alù, Experimental verification of three-dimensional plasmonic cloaking in free-space, New J. Phys. **14**, 013054 (2012).

[12] Z. H. Jiang and D. H. Werner, Exploiting metasurface anisotropy for achieving near-perfect low-profile cloaks beyond the quasistatic limit, J. Phys. D: Appl. Phys. **46**, 505306 (2013).

[13] N. M. Estakhri and A. Alù, Ultra-thin unidirectional carpet cloak and wavefront reconstruction with graded metasurfaces, IEEE Antennas Wireless Propag. Lett. **13**, 1775 (2014).

[14] X. Ni, Z. J. Wong, M. Mrejen, Y. Wang, and X. Zhang, An ultrathin invisibility skin cloak for visible light, Science **349**, 1310 (2015).

[15] Y. Yang, L. Jing, B. Zheng, R. Hao, W. Yin, E. Li, C. M. Soukoulis, and H. Chen, Full-polarization 3D metasurface cloak with preserved amplitude and phase, Adv. Mater. **28**, 6866 (2016).

[16] B. Orazbayev, N. M. Estakhri, A. Alù, and M. Beruete, Experimental demonstration of metasurface-based ultrathin carpet cloaks for millimeter waves, Adv. Opt. Mater. **5**, 1600606 (2017).

[17] D.-H. Kwon, Lossless tensor surface electromagnetic cloaking for large objects in free space, Phys. Rev. B **98**, 125137 (2018).

[18] W. X. Jiang and T. J. Cui, Radar illusion via metamaterials, Phys. Rev. E **83**, 026601 (2011).

[19] F. Yang, Z. L. Mei, W. X. Jiang, and T. J. Cui, Electromagnetic illusion with isotropic and homogeneous materials through scattering manipulation, J. Opt. **17**, 105610 (2015).

[20] S. Vellucci, A. Monti, A. Toscano, and F. Bilotti, Scattering Manipulation and Camouflage of Electrically Small Objects through Metasurfaces, Phys. Rev. Appl. **7**, 034032 (2017).

[21] Z. H. Jiang and D. H. Werner, Quasi-three-dimensional angle-tolerant electromagnetic illusion using ultrathin metasurface coatings, Adv. Funct. Mater. **24**, 7728 (2014).

[22] R. Wang, B.-Z. Wang, Z.-S. Gong, and X. Ding, Creation of an arbitrary electromagnetic illusion using a planar ultrathin metasurface, IEEE Photon. J. **9**, 4600809 (2017).

[23] S. R. Biswas, C. E. Gutiérrez, A. Nemilentsau, I.-H. Lee, S.-H. Oh, P. Avouris, and T. Low, Tunable Graphene Metasurface Reflectarray for Cloaking, Illusion, and Focusing, Phys. Rev. Appl. **9**, 034021 (2018).

[24] M. Safari, H. Kazemi, A. Abdolali, M. Albooyeh, and F. Capolino, Illusion mechanisms with cylindrical metasurfaces: A general synthesis approach, Phys. Rev. B **100**, 165418 (2019).

[25] A. Epstein and G. V. Eleftheriades, Arbitrary power-conserving field transformations with passive lossless Omega-type bianisotropic metasurfaces, IEEE Trans. Antennas Propag. **64**, 3880 (2016).

[26] A. Epstein and G. V. Eleftheriades, Synthesis of Passive Lossless Metasurfaces Using Auxiliary Fields for Reflectionless Beam Splitting and Perfect Reflection, Phys. Rev. Lett. **117**, 256103 (2016).

[27] D.-H. Kwon and S. A. Tretyakov, Perfect reflection control for impenetrable surfaces using surface waves of orthogonal polarization, Phys. Rev. B **96**, 085438 (2017).

[28] D.-H. Kwon, Lossless scalar metasurfaces for anomalous reflection based on efficient surface field optimization, IEEE Antennas Wireless Propag. Lett. **17**, 1149 (2018).

[29] D.-H. Kwon, Modulated reactance surfaces for leaky-wave radiation based on complete aperture field synthesis, IEEE Trans. Antennas Propag. (2020), doi:10.1109/TAP.2020.2977748.

[30] C. A. Balanis, *Antenna Theory: Analysis and Design*, 4th ed. (Wiley, Hoboken, NJ, 2016).

[31] C. Pfeiffer and A. Grbic, Metamaterial Huygens' Surfaces: Tailoring Wave Fronts with Reflectionless Sheets, Phys. Rev. Lett. **110**, 197401 (2013).

[32] M. Selvanayagam and G. V. Eleftheriades, Discontinuous electromagnetic fields using orthogonal electric and magnetic currents for wavefront manipulation, Opt. Express **21**, 14409 (2013).

[33] A. Epstein and G. V. Eleftheriades, Huygens' metasurfaces via the equivalence principle: Design and applications, J. Opt. Soc. Am. B **33**, A31 (2016).

[34] J. Cheng, S. Jafar-Zanjani, and H. Mosallaei, All-dielectric ultrathin conformal metasurfaces: Lensing and cloaking applications at 532 nm wavelength, Sci. Rep. **6**, 38440 (2016).

[35] M. Selvanayagam and G. V. Eleftheriades, Experimental Demonstration of Active Electromagnetic Cloaking, Phys. Rev. X **3**, 041011 (2013).

[36] A. M. H. Wong and G. V. Eleftheriades, Experimental demonstration of the Huygens' box: Arbitrary waveform generation in a metallic cavity, in *Proceedings of 2018 IEEE Antennas Propag. Soc. Int. Symp.* (Boston, MA, 2018) pp. 1893–1894.

[37] D. L. Sounas, R. Fleury, and A. Alù, Unidirectional Cloaking based on Metasurfaces with Balanced Loss and Gain, Phys. Rev. Appl. **4**, 014005 (2015).

[38] B. H. Fong, J. S. Colburn, J. J. Ottusch, J. L. Visher, and D. F. Sievenpiper, Scalar and tensor holographic artificial impedance surfaces, IEEE Trans. Antennas Propag. **58**, 3212 (2010).

[39] A. M. Patel and A. Grbic, Modeling and analysis of printed-circuit tensor impedance surfaces, IEEE Trans. Antennas Propag. **61**, 211 (2013).

[40] G. Minatti, F. Caminita, E. Martini, M. Sabbadini, and S. Maci, Synthesis of modulated-metasurface antennas with amplitude, phase, and polarization control, IEEE Trans. Antennas Propag. **64**, 3907 (2016).